Composites Part B 171 (2019) 214–221

Contents lists available at ScienceDirect

Composites Part B

journal homepage: www.elsevier.com/locate/compositesb

Broadband microwave absorbing materials based on MWCNTs' electromagnetic wave filtering effect

An Ling [a,b,c], Guoguo Tan [a,b,*], Qikui Man [a,b,**], Yaxin Lou [a,b], Shuwen Chen [a,b], Xisheng Gu [a,b], Run-Wei Li [a,b], Jing Pan [c], Xincai Liu [c]

[a] *Key Laboratory of Magnetic Materials and Devices, Ningbo Institute of Materials Technology & Engineering, Chinese Academy of Sciences, Ningbo, Zhejiang, 315201, China*

[b] *Zhejiang Province Key Laboratory of Magnetic Materials and Application Technology, Ningbo Institute of Materials Technology & Engineering, Chinese Academy of Sciences, Ningbo, Zhejiang, 315201, China*

[c] *School of Materials Science and Chemical Engineering, Ningbo University, Ningbo, 315211, China*

A R T I C L E I N F O

Keywords:
Microwave absorbing materials
Broadband
Carbon nanotubes
Filtering layer
Selective filtering effect

A B S T R A C T

Broadband microwave absorbing materials with a multilayer structure based on multi-walled carbon nanotubes (MWCNTs) as a filtering layer has been designed. The absorption curves of the multilayer structure change from a single peak to double peaks after the addition of the filtering layer. As a result, the effective microwave absorption bandwidth is broadened to 12.6 GHz with a total thickness of 2.3 mm. Normalized power flow and power loss distribution maps at fixed frequencies were analyzed by CST simulator. The broadening of the microwave absorption bandwidth is attributed to the electromagnetic wave selective filtering effect of the MWCNTs which contribute to impedance matching and microwave absorption at different frequencies.

1. Introduction

With the rapid development of electronic and communication technologies, the high density of electromagnetic waves (EMWs) with various frequencies have been widely applied in radar detection, wireless communication and electronic devices [1–4]. The electromagnetic radiation has resulted in a new kind of pollution, and electromagnetic compatibility also remains a key issue to be solved [5,6]. Compared with electromagnetic interference shielding materials, microwave absorption materials (MAMs) closely focus on absorption and dissipation inside rather than shielding capability [7–11]. To eliminate the detrimental effects of EMWs emerging from telecommunication and electronic equipment, high-performance MAMs with considerable effective absorption bandwidth (EAB, reflection loss less than −10 dB) is demanded [12–14]. On the on hand, many novel MAMs have been put forward, such as ferrite [15,16], magnetic metal nanocomposites [17,18], ceramics [19,20], carbon materials [21–23], to improve the performance of microwave absorbers. On the other hand, structural designs have been applied to broaden the absorption bandwidth in many literature [24–27]. Absorber with broader absorption band, lighter weight and superior performance for a fixed thickness is crucial to practical application.

Recently, multilayer structure microwave absorbers with large EAB have been studied intensively [28–35]. Jaeho [29] reported an absorber composed of a dielectric layer, resistive layer, and another dielectric-absorbing layer. The sandwich absorber exhibited a reflection loss (RL) below −10 dB from 4.7 to 13.7 GHz and a maximum RL was about −22.3 dB at 11.8 GHz. Wang [36] had designed a sandwiched structure absorber with a thin amorphous alloy slice between carbonyl iron (CI) composites, achieving two RL peaks and broadening the absorption band significantly. EAB is expanded by adjusting frequencies of two peaks which are related to thicknesses of magnetic layers. Zhang [37] presented a double-layer composite composed of Mn–Zn ferrite, achieving an effective absorption at 11.4–18 GHz.

Herein, we demonstrate a novel broadband high-performance microwave absorber with multilayer structure made by matching, filtering and absorption layers. Carbon materials are widely applied in electrical related field for high conductive characteristic, permittivity and high

* Corresponding author. Key Laboratory of Magnetic Materials and Devices, Ningbo Institute of Materials Technology & Engineering, Chinese Academy of Sciences, Ningbo, Zhejiang, 315201, China.

** Corresponding author. Zhejiang Province Key Laboratory of Magnetic Materials and Application Technology, Ningbo Institute of Materials Technology & Engineering, Chinese Academy of Sciences, Ningbo, Zhejiang, 315201, China.

E-mail address: kant01@126.com (G. Tan).

https://doi.org/10.1016/j.compositesb.2019.04.034
Received 8 January 2019; Received in revised form 15 April 2019; Accepted 29 April 2019
Available online 30 April 2019

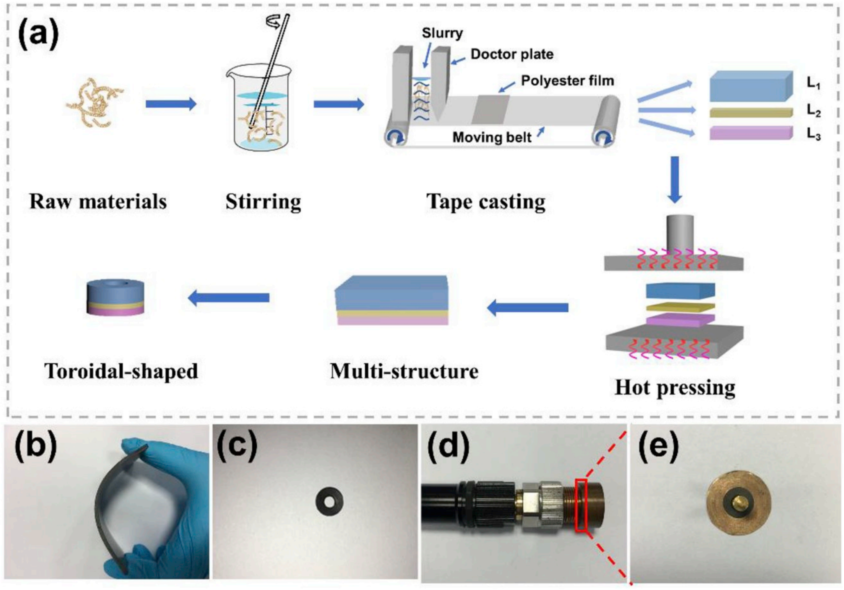

Fig. 1. (a) Schematic illustration of the fabrication of toroidal-shaped sample; (b) photograph of the flexible plate; (c) toroidal-shaped specimen; (d and e) S11-short for measuring reflection loss and sample placement with copper plate.

specific surface area [38–42]. Among carbon materials, carbon nanotubes (CNTs) are used for microwave absorption to broaden bandwidth and enhance absorption ability, on account of its remarkable properties, including low density, high permittivity and fibrous structure [43,44]. The MWCNTs layer with the filtering effect is applied to separate different frequency EMWs, showing a distinct reflection for high-frequency EMWs and transmission effect for low-frequency EMWs. Multilayer absorber in this paper generates different distribution of loss at different frequency EMWs. The MWCNTs layer between two magnetic particles results in two absorption peaks which drastically broaden the EAB, and CI/MWCNTs/$Ce_2Fe_{17}N_{3-\delta}$ multilayer absorber exhibits a large EAB reaching 12.6 GHz (5.4–18 GHz). The filtering effect of the MWCNTs layer is discussed with power flow density and power loss by CST simulator. The mechanism of the broadened absorption bandwidth is attributed to reflection and transmission at different frequencies, which contribute to dual impedance matching.

2. Experimental details

The magnetic powders were mixed with polyurethane (PU) and stirred to the slurry status with various percentage contents, as shown in Fig. 1a. The CI particles were uniformly mixed with a volume percentage of 38% (Cyclohexanone used as solution), and the slurry of 30% weight fraction of MWCNTs as well as 30% volume fraction of $Ce_2Fe_{17}N_{3-\delta}$ [45] was made with the same method. Afterwards, the slurry was poured into the feeding inlet of the tape casting machine and crushed by the doctor plate. The layer was drawn to the drying area and arid for 8 h at 70 °C. The layers were fabricated through this process and behaved flexible feature, as shown in Fig. 1b. Then, plates with three-layer structure were pressed by the hot-pressing machine under 80 °C and 2 tons of pressure. The toroidal-shaped samples were punched with outer and inner diameter of 7.00 mm and 3.04 mm, as shown in Fig. 1c. The RL of samples measured by coaxial method, namely the absorption of the absorbing layers with the perfect metal plate substrate (a thin copper plate was applied in this work, Fig. 1e, were obtained by measuring the S11-short using vector network analyzer (VNA), demonstrated in Fig. 1d.

The phases of the sample power were texted by X-ray diffraction (XRD, BRUKER D8 ADVANCE) using Cu-Kα radiation. Scanning electron microscope (SEM, FEI Quanta FEG 250) was carried out to observe morphology of sample power. Vibrating sample magnetometer (VSM, 7304, USA) was used to examine magnetic properties. Vector network analyzer (VNA, Agilent N5234A) in the range from 0.1 to 18 GHz was employed to measure the complex permittivity and permeability as well as reflection loss. Power loss and power flow were obtained by electromagnetic simulation software (CST STUDIO SUITE).

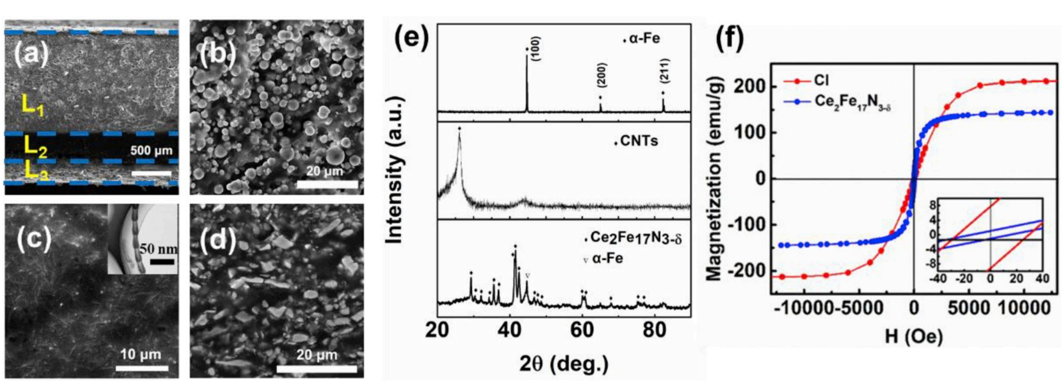

Fig. 2. SEM micrographs of the cross section images of (a) three-layer composite absorber, (b) CI/PU layer, (c) MWCNTs/PU layer and (d) $Ce_2Fe_{17}N_{3-\delta}$/PU layer; (e) XRD patterns of CI, MWCNTs and $Ce_2Fe_{17}N_{3-\delta}$; (f) Hysteresis loop of the CI and $Ce_2Fe_{17}N_{3-\delta}$ powder, the insert image is the local magnetization of the loops.

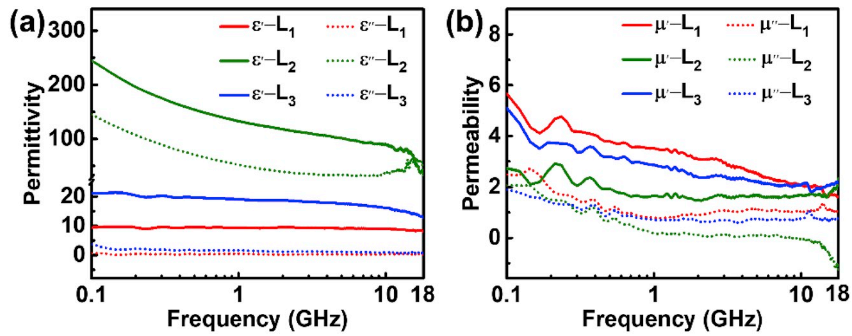

Fig. 3. Frequency dependence of (a) complex permittivity and (b) complex permeability of L_1, L_2 and L_3 composite.

3. Results and discussion

Fig. 2 show the cross-section images of CI/PU-MWCNTs/PU-$Ce_2Fe_{17}N_{3-\delta}$/PU multi-layer composite absorber with visible interface. The matching layer L_1 is presented in Fig. 2b, it is shown that the spherical CI particles are uniformly distributed in the PU matrix with a small particle diameter between 2 and 5 μm, which can reduce eddy current loss and obtain the higher permeability. Fig. 2c presents the randomly dispersed MWCNTs and porous network forming a conductive network in the layer L_2. MWCNTs shows a bamboo-like structure and diameter is near 10 nm, as shown in insert image of Fig. 2c. The $Ce_2Fe_{17}N_{3-\delta}$ magnetic powders in irregular shape were also homogeneously distributed in the matrix of PU, as shown in Fig. 2d. Fig. 2e displays XRD patterns of CI, MWCNTs and $Ce_2Fe_{17}N_{3-\delta}$ powders, respectively. Three peaks in CI pattern at ~44.7°, ~65.0° and ~82.3° are corresponding to (110), (200) and (211) crystallographic planes of α-Fe, respectively. The peak at ~26° can be ascribed to the (002) planes Only one peak can be found in XRD pattern of MWCNTs at 26°, corresponding (002). The XRD pattern of $Ce_2Fe_{17}N_{3-\delta}$ indicates the particles had a typical rhombohedral Th_2Zn_{17}-type structure [46] and few α-Fe phases. The soft-magnetic properties of CI and $Ce_2Fe_{17}N_{3-\delta}$ powders at room temperature are investigated, as shown in Fig. 2f. The values of saturation magnetization are 212 and 144 emu/g as well as the coercivity is 30 and 16 Oe, respectively. The rather high saturation magnetization and low coercivity can improve the properties of high-frequency magnetic loss [47], which have a positive effect on microwave absorption.

Fig. 3 presents complex permittivity ε and complex permeability μ of L_1, L_2 and L_3, including the real part and the imaginary part. The L_2 real part of permittivity decreases from 244.8 to 33.5 and the imaginary part of permittivity declines to 48.6 from 148.2 with frequency increasing from 0.1 GHz to 18 GHz simultaneously, as shown in Fig. 3a. Such high permittivity indicates that the skin depths in MWCNTs layer are more sensitive to the frequencies, providing a different transmission for various frequency regions. The composites of L_1 and L_3 maintain nearly constant real ε value of 20 and 10, respectively. The real and the imaginary parts of complex permeability μ for L_1 and L_3 decrease with frequency, as shown in Fig. 3b. Meanwhile, the matching layer L_1 and absorption layer L_3 display minor changes in the measured frequency range. And the imaginary part of permittivity is near zero which has almost no contribution to electric loss.

To investigate the electromagnetic wave absorption performance, the RL of EMWs can be calculated by the following equations [48,49] according to the transmission line theory.

$$Z_{in} = Z_0\sqrt{\frac{\mu_r}{\varepsilon_r}}\tanh j\frac{2\pi ft}{c}\sqrt{\mu_r\varepsilon_r} \quad (1)$$

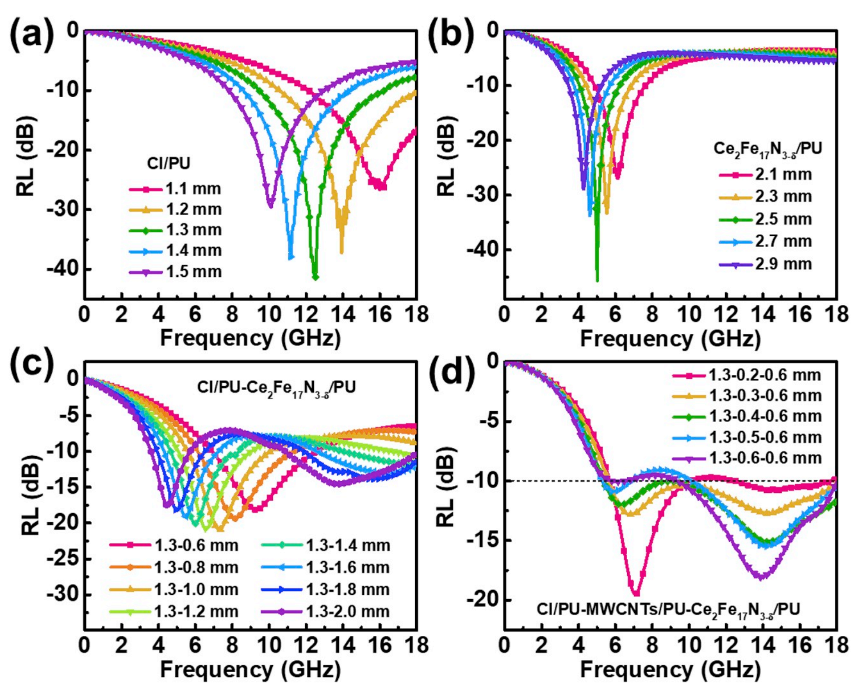

Fig. 4. RL curves of (a) L_1, (b) L_3, (c) L_1 and L_3, (d) L_1, L_2 and L_3 composites with different thicknessed.

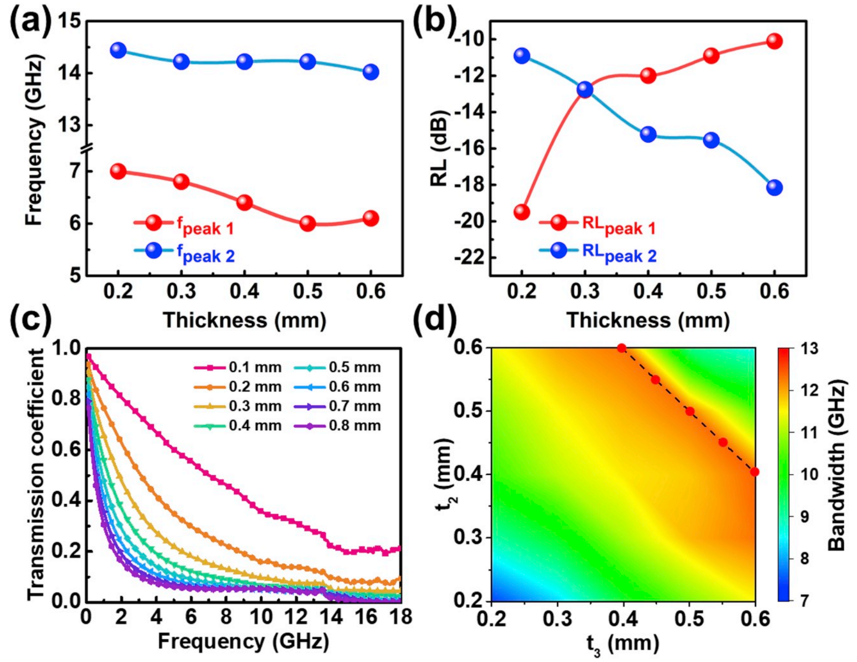

Fig. 5. Dependence of (a) absorption peak frequencies and (b) maximum RL value on thickness of L_2 layer, (c) transmission coefficient of different L_2 layer thicknesses and (d) EAB of different thicknesses of absorption L_2 and L_3 for a fixed matching layer with 1.3 mm; the red spot in a dotted line displays the maximum bandwidth of the results. (For interpretation of the references to color in this figure legend, the reader is referred to the Web version of this article.)

$$\mathrm{RL} = -20\lg\left|\frac{Z_{in} - Z_0}{Z_{in} + Z_0}\right| \tag{2}$$

Where Z_{in} is input impedance of the sample, Z_0 is the impedance of air, ε_r and μ_r are the relative complex permittivity and relative complex permeability, f is frequency, t is the thickness of the sample and c is the velocity of light.

The RL of matching layer L_1 at various thicknesses was measured, as shown in Fig. 4a. The peak shifts from 16 GHz to 10.1 GHz as the thickness increased from 1.1 mm to 1.5 mm. There is only one strong absorption peak of the RL curve in the measured frequency range. The maximum absorption reaches −40.7 dB at 12.4 GHz and the EAB is only 6.7 GHz when the thickness is 1.3 mm. The results confirm that CI/PU composite shows excellent microwave absorption feature at higher frequencies. Fig. 4b exhibits the RL curves of the L_3 layer at various thicknesses, appearing an EAB of ~2.2 GHz and strongest absorption with −45.6 dB at 4.5 GHz. Since single component layers cannot achieve the purpose of broad bandwidth, microwave absorber with two layers was applied. To ensure the absorber to be as thin as possible, the fixed L_1 is 1.3 mm, and the RL curves are obtained by altering thickness of L_3, as shown in Fig. 4c. Compared with single layer, double-layer absorber obtains two absorption peaks in the measured frequency range as well as wider effective absorption region up to ~10 GHz. Two RL peaks both shifts to lower frequencies with thickness increasing, and the value of RL cannot reach −10 dB in frequency range of 6–11 GHz. To promote the absorption performance, L_2 was employed between the matching layer and absorption layer, and the RL curves is showed in Fig. 4d. When the thickness of L_2 layer is up to 0.3 mm, two peaks are obtained evidently and EAB reaches 12.3 GHz. Compared with two-layer absorbers, three-layer absorbers show superior absorbing performances in the middle frequency range.

The dependence of peak frequencies and maximum RL values on L_2 thickness are analyzed as showed in Fig. 5a and b. The values of peak 2 (absorption peak at higher frequency) is located at near 14 GHz, and the peak 1 (absorption peak at lower frequency) shifts from 7 GHz to 6.1 GHz which indicate it is more sensible to the filtering layer thickness. It demonstrates that the L_2 layer between two magnetic composite layers exhibits different affect to higher and lower frequencies. The maximum RL value reaches −19.5 dB when the MWCNTs layer is 0.2 mm. Two absorption peaks in the measured frequency range reach −10dB when the thicknesses are below 0.6 mm, as shown in Fig. 5b. The transmission coefficient (T) of MWCNTs layers at different thicknesses were calculated by the equation of $T = |S_{21}|^2$ [50,51], as shown in Fig. 5c. The curves show that transmission coefficients of EMWs decrease with frequency under a fixed thickness. When the EMWs reach the surface of MWCNTs layer, high-frequency waves are reflected dramatically and a small fraction of them can travel through the layer. The transmission coefficients sharply declined with the growing thickness of MWCNTs layer. When the thickness exceeds 0.4 mm, the transmission coefficients show a faint fall with the increasing thickness. Fig. 5d shows the EAB of different thicknesses of L_2 and L_3 for a fixed L_1 with 1.3 mm in thickness. From the distribution of bandwidth, it can be observed that the area with the largest bandwidth is linearly arranged (Red spot on dotted line), indicating that the total thickness of the absorber is approximately 2.3 mm. In other words, effective absorption bandwidth is related to total thickness of the absorber.

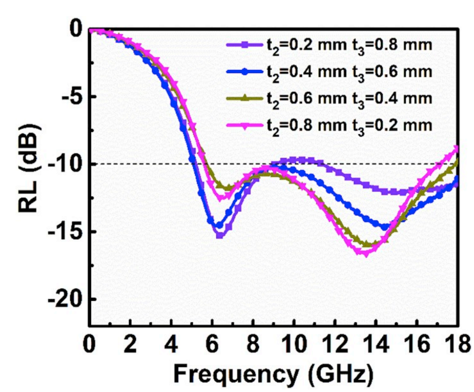

Fig. 6. Frequency versus RL values at different t_2 and t_3 with fixed t_1 at 1.3 mm.

The RL with various t_2 and t_3 with a fixed t_1 was also studied, as

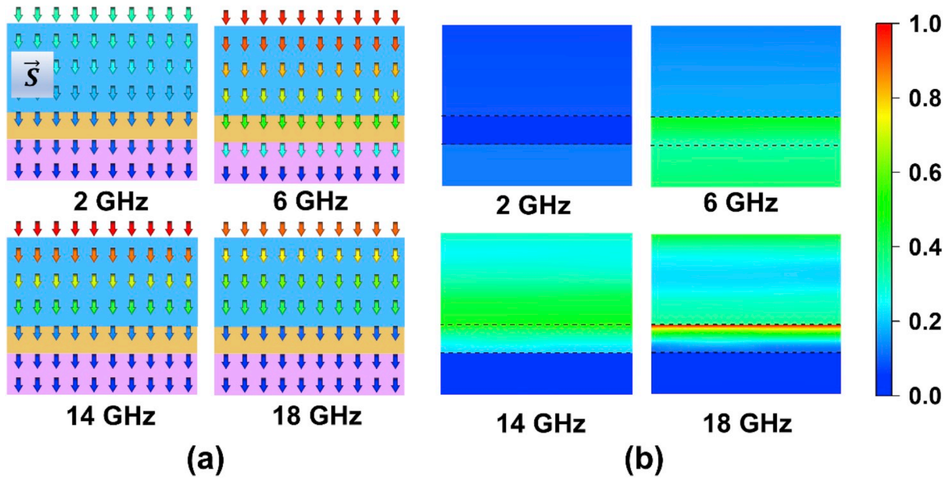

Fig. 7. Normalized (a) power flow and (b) power loss distribution maps at fixed frequencies (2 GHz, 6 GHz, 14 GHz and 18 GHz) on x-z cross-section.

shown in Fig. 6. When t_2 is 0.2 mm, the reflections of higher frequencies are unable to meet the demand, causing the RL value in the 9–11 GHz frequency range cannot reach −10 dB and the bandwidth is only 10.5 GHz. With t_2 increasing, the absorption peak at lower frequencies shifts slightly, and RL in the 9–11 GHz frequency region are enhanced significantly. This indicates that tunable thickness of t_2 and t_3 leads to the enhanced absorption performance at higher frequency and broaden EAB. The superior performance is obtained under the condition of $t_1 = 1.3$ mm, $t_2 = 0.4$ mm and $t_3 = 0.6$ mm. The maximum absorption value reaches −15dB and the EAB is 12.6 GHz. The EAB are related to the thickness of whole absorber and the matching layer. Generally, the microwave absorption is remarkably influenced by the impedance matching condition. The impedance matching condition at lower frequency is improved by the addition of the MWCNTs layer. Meanwhile, the EMWs reflected by MWCNTs layer led to an impedance condition with matching layer. The EMWs were reflected completely due to the metal plate and is eliminated by the absorber.

To investigate the absorption mechanism of the sandwich absorbers, the power flow density at four fixed frequencies were calculated by the following equations:

$$\vec{S} = \vec{E} \times \vec{H} \tag{3}$$

$$\vec{S}_{av} = \frac{1}{T}\int_0^T \vec{S}\,dt = \frac{1}{2}Re\left[\vec{E} \times \vec{H}\right] \tag{4}$$

The directions and magnitudes of the power flow are marked with arrows and color fill, as shown in Fig. 7a. The values of power flow density are simulated using CST at different frequency when t_1, t_2 and t_3 is 0.6 mm, 0.4 mm and 1.3 mm, respectively. The power flow of the EMWs decline with increasing depth and maintains the same direction. The gradual reduction of the power flow confirms the absorbing ability of the absorber. What's more, contrast to 2 GHz, the values of power flow at higher frequencies are larger on the interface between air and absorber. This phenomenon indicates that absorber has stronger attenuation capability to high-frequency EMWs. As the frequencies increased, the power flow in the L_3 shows a small value, resulting from the reflection effect to high-frequency EMWs of MWCNTs. The addition of the MWCNTs layer leads to different transmission effect on various frequencies EMWs.

To further investigate the contribution of each layer to attenuation, normalized power loss was calculated, revealed in Fig. 7b. The power loss can be calculated by the following equation:

$$P_{loss} = -\nabla \cdot Re\left[\vec{E} \times \vec{H}\right] = -2\nabla \cdot \vec{S}_{av} \tag{5}$$

The power loss is mainly concentrated on the L_3 at 2 GHz and 6 GHz. The EMWs at lower frequencies have an unobstructed or less-obtrusive transmission through the MWCNTs layer, leading to power loss in each layer in absorber. The absorption peak appears at 6 GHz, which means that the designed absorber obtains strong absorption at this frequency, corresponding to the green color fill. With the increase of frequency, high-frequency EMWs are dramatically reflected the MWCNTs layer. The power loss mainly emerges in the matching layer and filtering layer. The EMWs power loss of 14 GHz indicates that CI had an excellent absorbing ability at this frequency range. At 18 GHz, the matching layer has poor absorption, corresponding to the reflection loss curve in Fig. 4a, while the MWCNTs have a large dielectric loss, so the energy loss is concentrated on the surface of the MWCNTs layer. Meanwhile, MWCNTs are dispersed uniformly in the polyurethane, and 3D conductive micro circuit MWCNTs networks are formed to cause attenuation. And multi-reflection of the EMWs emerges, which leads to the dramatic loss on

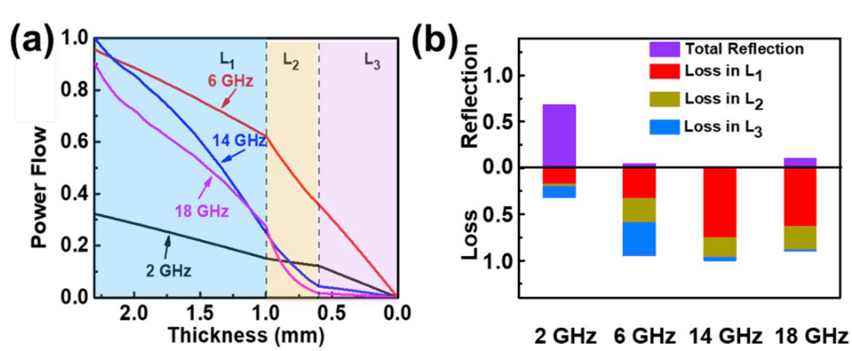

Fig. 8. (a) Numerical power flow details in the absorber and (b) loss percentages in each layer and reflection on the interface between L_1 and air at different frequencies.

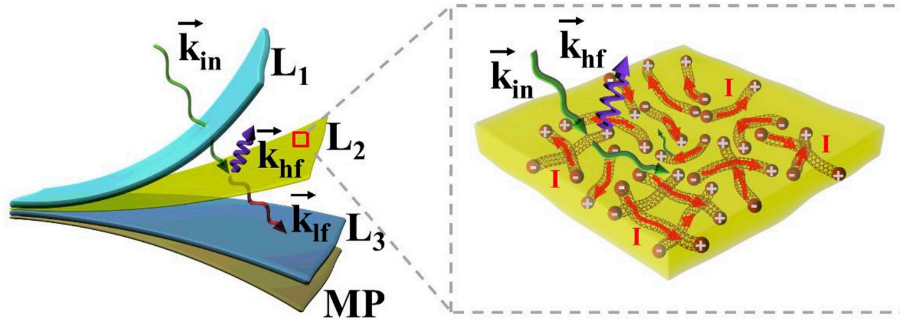

Fig. 9. Schematic diagram of action mechanism of MWCNTs.

Table 1
Microwave absorption performance of representative multilayer structure.

Ref.	Materials	Thickness (mm)	Bandwidth (frequency range) (GHz)
[27]	graphene nanosheets/epoxy resin	3.9	5.4 (5.0–6.8, 13.2–16.8)
[29]	0.15 MWNT E-glass/6.6 MWNT cotton fabric/0.5 MWNT E-glass	6	9.0 (4.7–13.7)
[30]	CI/CB	4	1.2 (4.9–6.1)
[31]	Epoxy glass fiber/RGO/Epoxy glass fiber	3.2	10.0 (8.0–18.0)
[33]	CI/$CoFe_2O_4$	2.9	9.4 (8.6–18.0)
[35]	CI/$BaTiO_3$	1.4	4.0 (10.8–14.8)
[37]	mortar with silica fume/Mn–Zn ferrite	30.0	6.6 (11.4–18.0)
[52]	1.98OMC/2.99OMC	2.0	5.4 (8.9–14.3)
[53]	Glass balls/ferrite	3.3	3.8 (8.0–11.8)
[54]	E-glass/epoxy nanocomposites	5.5	10.4 (6.0–16.4)
[55]	Hexagonal ferrite/CI	2.0	7.0 (5.0–12.0)
[56]	5.5 CB doped SiO_{2f}/15 CB doped SiO_2	1.6	3.9 (14.1–18.0)
[57]	CI/barium hexaferrite	2.3	5.3 (5.6–10.8)
[58]	$Co_{0.2}Ni_{0.4}Zn_{0.4}Fe_2O_4$/RGO	2.5	6.0 (12.0–18.0)
[59]	CNT/EG/$BaFe_{12}O_{19}$	1.0	4.2 (12.2–16.4)
This work	CI/MWCNTs/$Ce_2Fe_{17}N_{3-\delta}$	2.3	12.6 (5.4–18.0)

the surface of MWCNTs layer. In addition, the scattered MWCNTs on the surface of L_2 may generate dipolar oscillation and contribute to EMWs loss.

Normalized power flow was also calculated by the maximum value of simulated results. And the contributions of each layer are displayed in Fig. 8a. The statistics of loss percentages in each layer and reflection are shown in Fig. 8b. In lower frequency region, reflection occupied the majority of the EMWs, reaching 0.71, and weak absorption is obtained. For the EMWs at 6 GHz, the loss evenly distributed in the three layers indicating the whole absorber participates in the absorption. For the higher frequencies, the power flow on the surface indicated a strong absorption in the absorber. The power flow at 14 GHz and 18 GHz decrease to 0.74 and 0.62 respectively in the absorption layer. And little absorption happens in the L_3, meaning that MWCNTs layer have the excellent reflection effect on high-frequency EMWs. EMWs are dramatically absorbed at 6 GHz and 14 GHz and little EMWs is reflected, corresponding two peaks in the RL curve, meaning the good impedance and attenuation are reached in these conditions.

The existence of the MWCNTs layer contributes to the absorption in four aspects (see Fig. 9). For the main factor, high-frequency EMWs are reflected by MWCNTs layer, and little of them hindered effect on the lower frequencies. This leads to the decoupling of higher and lower frequency EMWs and provides the possibility to obtain broadband absorption. Secondly, MWCNTs are dispersed uniformly in the polyurethane, and the 3D conductive micro circuit MWCNTs networks are formed. And multi-reflection of the EMWs emerges, which leads to the dramatic loss on the surface of MWCNTs layer. Due to the high content of the MWCNTs padding, the amount of loss caused by multiple reflections of high-frequencies EMWs is considerable. In addition, many defects, such as lattice distortion and vacancy in the bamboo-like multi-walled carbon nanotubes, enhanced the electrical loss due to the orientation polarization under the action of the microwave electric field. And the scattered MWCNTs on the surface of L_2 may generate dipolar oscillation and electric dipole will be formed at both ends of MWCNTs under the condition of EMWs, which may contribute to EMWs loss.

In Table 1, comparisons of multi-layer structure microwave absorbers in previous publications and this work are listed. The three layers in this work broaden the absorption bandwidth significantly. The enhancement of the bandwidth is considered to benefit from the selective transmission characteristics of the filtering layer.

4. Conclusions

Through altering the thickness of each layer, the reflection loss and the mechanism of a three-layer absorber composed of CI/MWCNTs/$Ce_2Fe_{17}N_{3-\delta}$ have been studied. Results show that the superior absorption performance is realized under conditions of $t_1 = 1.3$ mm, $t_2 = 0.4$ mm and $t_3 = 0.6$ mm, and the maximum EAB reaches 12.6 GHz. MWCNTs layer takes a critical effect on the broadening of effective bandwidth and the reduction of thickness. The variation of power flow and power loss at different frequencies further indicates that MWCNTs plays a key role in low-pass and high-reflect effect. It has been demonstrated that MWCNTs/PU composite is an effective filtering material to improve multi-layer absorber capability.

Acknowledgments

This work was supported by the Ningbo National Natural Science Foundation [grant number 2018A610079]; Zhejiang Provincial Natural Science Foundation [grant number LQ19E010001]; National Natural Science Foundation of China [grant number 51174121].

References

[1] Sun Y, Zhang J, Zong Y, Deng X, Zhao H, Feng J, et al. Crystalline-amorphous permalloy@iron oxide core–shell nanoparticles decorated on graphene as high-efficiency, lightweight, and hydrophobic microwave absorbents. ACS Appl Mater Interfaces 2019;11:6374–83.

[2] Wang L, Qiu H, Liang C, Song P, Han Y, Han Y, et al. Electromagnetic interference shielding MWCNT-Fe_3O_4@Ag/epoxy nanocomposites with satisfactory thermal conductivity and high thermal stability. Carbon 2019;141:506–14.

[3] Huang Y, Ji J, Chen Y, Li X, He J, Cheng X, et al. Broadband microwave absorption of $Fe_3O_4BaTiO_3$ composites enhanced by interfacial polarization and impedance matching. Compos B Eng 2019;163:598–605.

[4] Liu P, Zhang Y, Yan J, Huang Y, Xia L, Guang Z. Synthesis of lightweight N-doped graphene foams with open reticular structure for high-efficiency electromagnetic wave absorption. Chem Eng J 2019;368:285–98.

[5] Liu P, Huang Y, Yan J, Yang Y, Zhao Y. Construction of CuS nanoflakes vertically aligned on magnetically decorated graphene and their enhanced microwave absorption properties. ACS Appl Mater Interfaces 2016;8:5536–46.

[6] Zhong B, Wang C, Wen G, Yu Y, Xia L. Facile fabrication of boron and nitrogen co-doped carbon@Fe_2O_3/Fe_3C/Fe nanoparticle decorated carbon nanotubes three-dimensional structure with excellent microwave absorption properties. Compos B Eng 2018;132:141–50.

[7] Liang C, Qiu H, Han Y, Gu H, Song P, Wang L, et al. Superior electromagnetic interference shielding 3D graphene nanoplatelets/reduced graphene oxide foam/epoxy nanocomposites with high thermal conductivity. J Mater Chem C 2019;7:2725–33.

[8] Tang W, Lu L, Xing D, Fang H, Liu Q, Teh KS. A carbon-fabric/polycarbonate sandwiched film with high tensile and EMI shielding comprehensive properties: an experimental study. Compos B Eng 2018;152:8–16.

[9] Huangfu Y, Liang C, Han Y, Qiu H, Song P, Wang L, et al. Fabrication and investigation on the Fe_3O_4/thermally annealed graphene aerogel/epoxy electromagnetic interference shielding nanocomposites. Compos Sci Technol 2019;169:70–5.

[10] Liu P, Huang Y, Yan J, Zhao Y. Magnetic graphene@PANI@porous TiO_2 ternary composites for high-performance electromagnetic wave absorption. J Mater Chem C 2016;4:6362–70.

[11] Zheng X, Feng J, Zong Y, Miao H, Hu X, Bai J, et al. Hydrophobic graphene nanosheets decorated by monodispersed superparamagnetic Fe_3O_4 nanocrystals as synergistic electromagnetic wave absorbers. J Mater Chem C 2015;3:4452–63.

[12] Qin F, Brosseau C. A review and analysis of microwave absorption in polymer composites filled with carbonaceous particles. J Appl Phys 2012;111, 061301.

[13] Park K-Y, Lee S-E, Kim C-G, Han J-H. Fabrication and electromagnetic characteristics of electromagnetic wave absorbing sandwich structures. Compos Sci Technol 2006;66:576–84.

[14] Kuang B, Ning M, Wang L, Li J, Wang C, Hou Z, et al. Biopolymer nanofiber/reduced graphene oxide aerogels for tunable and broadband high-performance microwave absorption. Compos B Eng 2019;161:1–9.

[15] Ting T-H, Wu K-H. Synthesis, characterization of polyaniline/$BaFe_{12}O_{19}$ composites with microwave-absorbing properties. J Magn Magn Mater 2010;322:2160–6.

[16] Gandhi N, Singh K, Ohlan A, Singh DP, Dhawan SK. Thermal, dielectric and microwave absorption properties of polyaniline-$CoFe_2O_4$ nanocomposites. Compos Sci Technol 2011;71:1754–60.

[17] Ghasemi A, Sepelak V, Liu X, Morisako A. Microwave absorption properties of Mn-Co-Sn doped barium ferrite nanoparticles. IEEE Trans Magn 2009;45:2456–9.

[18] Li ZW, Yang ZH, Huang RF, Kong LB. Greatly enhanced permeability and expanded bandwidth for spinel ferrite composites with flaky fillers. IEEE Trans Microw Theory Tech 2010;58:2794–9.

[19] Qing Y, Zhou W, Luo F, Zhu D. Thin-thickness FeSiAl/flake graphite-filled Al_2O_3 ceramics with enhanced microwave absorption. Ceram Int 2017;43:870–4.

[20] Yang Z, Luo F, Hu Y, Zhu D, Zhou W. Dielectric and microwave absorption properties of TiAlCo ceramic fabricated by atmospheric plasma spraying. Ceram Int 2016;42:8525–30.

[21] Cao M-S, Yang J, Song W-L, Zhang D-Q, Wen B, Jin H-B, et al. Ferroferric oxide/multiwalled carbon nanotube vs polyaniline/ferroferric oxide/multiwalled carbon nanotube multiheterostructures for highly effective microwave absorption. ACS Appl Mater Interfaces 2012;4:6949–56.

[22] Wang G, Gao Z, Tang S, Chen C, Duan F, Zhao S, et al. Microwave absorption properties of carbon nanocoils coated with highly controlled magnetic materials by atomic layer deposition. ACS Nano 2012;6:11009–17.

[23] Li Z, Li X, Zong Y, Tan G, Sun Y, Lan Y, et al. Solvothermal synthesis of nitrogen-doped graphene decorated by superparamagnetic Fe_3O_4 nanoparticles and their applications as enhanced synergistic microwave absorbers. Carbon 2017;115:493–502.

[24] Zhou Q, Yin X, Ye F, Liu X, Cheng L, Zhang L. A novel two-layer periodic stepped structure for effective broadband radar electromagnetic absorption. Mater Des 2017;123:46–53.

[25] Li W, Wei J, Wang W, Hu D, Li Y, Guan J. Ferrite-based metamaterial microwave absorber with absorption frequency magnetically tunable in a wide range. Mater Des 2016;110:27–34.

[26] Sun H, Che R, You X, Jiang Y, Yang Z, Deng J, et al. Cross-stacking aligned carbon-nanotube films to tune microwave absorption frequencies and increase absorption intensities. Adv Mater 2014;26:8120–5.

[27] Min D, Zhou W, Qing Y, Luo F, Zhu D. Single-layer and double-layer microwave absorbers based on graphene nanosheets/epoxy resin composite. Nano 2017;12:1750089.

[28] Luo H, Chen F, Wang X, Dai W, Xiong Y, Yang J, et al. A novel two-layer honeycomb sandwich structure absorber with high-performance microwave absorption. Compos Part A Appl Sci Manuf 2019;119:1–7.

[29] Choi J, Jung H-T. A new triple-layered composite for high-performance broadband microwave absorption. Compos Struct 2015;122:166–71.

[30] Meng W, Yuping D, Shunhua L, Xiaogang L, Zhijiang J. Absorption properties of carbonyl-iron/carbon black double-layer microwave absorbers. J Magn Magn Mater 2009;321:3442–6.

[31] Ye F, Song C, Zhou Q, Yin X, Han M, Li X, et al. Broadband microwave absorbing composites with a multi-scale layered structure based on reduced graphene oxide film as the frequency selective surface. Materials 2018;11:1771.

[32] He L-H, Deng L-W, Luo H, He J, Li Y-H, Xu Y-C, et al. Broadband microwave absorption properties of polyurethane foam absorber optimized by sandwiched cross-shaped metamaterial. Chinese Phys B 2018;27:127801.

[33] Liu Y, Liu X, Wang X. Double-layer microwave absorber based on $CoFe_2O_4$ ferrite and carbonyl iron composites. J Alloy Comp 2014;584:249–53.

[34] Li W, Jin H, Zeng Z, Zhang L, Zhang H, Zhang Z. Flexible and easy-to-tune broadband electromagnetic wave absorber based on carbon resistive film sandwiched by silicon rubber/multi-walled carbon nanotube composites. Carbon 2017;121:544–51.

[35] Qing Y, Zhou W, Luo F, Zhu D. Optimization of electromagnetic matching of carbonyl iron/BaTiO3 composites for microwave absorption. J Magn Magn Mater 2011;323:600–6.

[36] Wang T, Wang P, Wang Y, Qiao L. A broadband far-field microwave absorber with a sandwich structure. Mater Des 2016;95:486–9.

[37] Zhang X, Sun W. Microwave absorbing properties of double-layer cementitious composites containing Mn–Zn ferrite. Cement Concr Compos 2010;32:726–30.

[38] Liu P, Yan J, Gao X, Huang Y, Zhang Y. Construction of layer-by-layer sandwiched graphene/polyaniline nanorods/carbon nanotubes heterostructures for high performance supercapacitors. Electrochim Acta 2018;272:77–87.

[39] Liu P, Yang M, Zhou S, Huang Y, Zhu Y. Hierarchical shell-core structures of concave spherical NiO nanospines@carbon for high performance supercapacitor electrodes. Electrochim Acta 2019;294:383–90.

[40] Ning M, Li J, Kuang B, Wang C, Su D, Zhao Y, et al. One-step fabrication of N-doped CNTs encapsulating M nanoparticles (M = Fe, Co, Ni) for efficient microwave absorption. Appl Surf Sci 2018;447:244–53.

[41] Feng J, Zong Y, Sun Y, Zhang Y, Yang X, Long G, et al. Optimization of porous FeNi3/N-GN composites with superior microwave absorption performance. Chem Eng J 2018;345:441–51.

[42] Luo C, Jiao T, Gu J, Tang Y, Kong J. Graphene shield by SiBCN ceramic: a promising high-temperature electromagnetic wave-absorbing material with oxidation resistance. ACS Appl Mater Interfaces 2018;10:39307–18.

[43] Dang Z-M, Yao S-H, Yuan J-K, Bai J. Tailored dielectric properties based on microstructure change in $BaTiO_3$-carbon nanotube/polyvinylidene fluoride three-phase nanocomposites. J Phys Chem C 2010;114:13204–9.

[44] Shao Y, Lu W, Chen H, Xiao JQ, Qiu Y, Chou T-W. Flexible ultra-thin Fe_3O_4/MnO_2 core-shell decorated CNT composite with enhanced electromagnetic wave absorption performance. Compos B Eng 2018;144:111–7.

[45] Gu X, Tan G, Chen S, Man Q, Chang C, Wang X, et al. Microwave absorption properties of planar-anisotropy $Ce_2Fe_{17}N_{3-\delta}$ powders/Silicone composite in X-band. J Magn Magn Mater 2017;424:39–43.

[46] Coey JMD, Smith PAI. Magnetic nitrides. J Magn Magn Mater 1999;200:405–24.

[47] Shirakata Y, Hidaka N, Ishitsuka M, Teramoto A, Ohmi T. High permeability and low loss Ni–Fe composite material for high-frequency applications. IEEE Trans Magn 2008;44:2100–6.

[48] Ning M-Q, Lu M-M, Li J-B, Chen Z, Dou Y-K, Wang C-Z, et al. Two-dimensional nanosheets of MoS_2: a promising material with high dielectric properties and microwave absorption performance. Nanoscale 2015;7:15734–40.

[49] Feng J, Pu F, Li Z, Li X, Hu X, Bai J. Interfacial interactions and synergistic effect of CoNi nanocrystals and nitrogen-doped graphene in a composite microwave absorber. Carbon 2016;104:214–25.

[50] Song W-L, Cao M-S, Lu M-M, Bi S, Wang C-Y, Liu J, et al. Flexible graphene/polymer composite films in sandwich structures for effective electromagnetic interference shielding. Carbon 2014;66:67–76.

[51] Saini P, Choudhary V, Vijayan N, Kotnala RK. Improved electromagnetic interference shielding response of poly(aniline)-coated fabrics containing dielectric and magnetic nanoparticles. J Phys Chem C 2012;116:13403–12.

[52] Wu H, Wang L, Guo S, Shen Z. Double-layer structural design of dielectric ordered mesoporous carbon/paraffin composites for microwave absorption. Appl Phys A 2012;108:439–46.

[53] Han M, Ou Y, Deng L. Microwave absorption properties of double-layer absorbers made of NiCoZn ferrites and hollow glass microspheres electroless plated with FeCoNiB. J Magn Magn Mater 2009;321:1125–9.

[54] Khurram A, Raza MA, Zhou P, Subhani T. A study of the nanocomposite sandwich structures for broadband microwave absorption and flexural strength. J Sandw Struct Mater 2016;18:739–53.

[55] Oikonomou A, Giannakopoulou T, Litsardakis G. Design, fabrication and characterization of hexagonal ferrite multi-layer microwave absorber. J Magn Magn Mater 2007;316:e827–30.

[56] Dong J, Zhou W, Qing Y, Gao L, Duan S, Luo F, et al. Dielectric and microwave absorption properties of CB doped SiO_{2f}/PI double-layer composites. Ceram Int 2018;44:14007–12.

[57] Ren X, Fan H, Cheng Y. Microwave absorption properties of double-layer absorber based on carbonyl iron/barium hexaferrite composites. Appl Phys A-Mater 2016; 122.

[58] Liu P, Ng VMH, Yao Z, Zhou J, Lei Y, Yang Z, et al. Microwave absorption properties of double-layer absorbers based on $Co_{0.2}Ni_{0.4}Zn_{0.4}Fe_2O_4$ ferrite and reduced graphene oxide composites. J Alloy Comp 2017;701:841–9.

[59] Zhao T, Jin W, Ji X, Yan H, Jiang Y, Dong Y, et al. Synthesis of sandwich microstructured expanded graphite/barium ferrite connected with carbon nanotube composite and its electromagnetic wave absorbing properties. J Alloy Comp 2017;712:59–68.